Nonlinear Amplification of Stationary Rossby Waves Near Resonance. Part I.

P. MALGUZZI

CNR-FISBAT, Bologna, Italy

A. SPERANZA, A. SUTERA, AND R. CABALLERO

Universita' di Camerino, Camerino, Italy

(Manuscript received 25 July 1994, in final form 13 July 1995)

ABSTRACT

The authors search the stationary solutions of the barotropic vorticity equation in spherical coordinates by numerically solving the equations with the Newton–Keller pseudoarclength continuation method. The solutions consist of planetary-scale Rossby waves superimposed on zonal wind profiles and forced by sinusoidal orography in near-resonance conditions. By varying the zonal wind strength across resonance, it is shown that multiple solutions with different wave amplitudes can be found: for small forcing and dissipation, the solution curve is the well-known bended resonance. The comparison between numerical results and theoretical predictions by a previously developed weakly nonlinear theory is successfully attempted.

The authors then extend the barotropic, weakly nonlinear theory to stationary Rossby waves forced by large-scale orography and dissipated by Ekman friction at the surface, in the framework of the quasigeostrophic model continuous in the vertical direction. The waves are superimposed on vertical profiles of zonal wind and stratification parameters taken from observations of the wintertime Northern Hemisphere circulation. In near-resonant conditions, the weakly nonlinear theory predicts multiple amplitude equilibration of the eddy field for a fixed vertical profile of the zonal wind. The authors discuss the energetics of the stationary waves and show that the form drag and Ekman dissipation can be made very small even if realistic values of the parameters are taken, at variance with the barotropic case.

This model is proposed as the theoretical base for such phenomena as atmospheric blocking, bimodality, and weather regimes.

1. Introduction

In the last decade we have investigated many different aspects of low-frequency variability: (i) the estimation of probability density for different parameters, both in the real atmosphere (Hansen and Sutera 1986, 1987; Benzi and Speranza 1989) and in simulation models (Hansen and Sutera 1990; Hansen et al. 1991); (ii) the dynamical nature of flow patterns corresponding to maxima in estimates of probability densities (Hansen 1988); and (iii) the physical nature of instabilities driving atmospheric circulation from one pattern to the other and the construction of a hierarchy of "minimal models" reproducing the observed statistics (Benzi et al. 1986a,b; Benzi et al. 1988). In this process we had to analyze the nature of confinement in the meridional plane of ultralong waves (Pandolfo and Sutera 1991; Benzi and Malguzzi 1992), which is at the basis of the resonant amplification that plays a key role in our theory on nonlinear bending (Benzi et al. 1986a, hereafter referred to as BMSS).

In this paper we will not readdress the questions above. Our purpose is instead to move further toward the identification of the physical mechanisms responsible for some particular properties of observed ultralong planetary waves. In particular, we consider the fact that observed patterns of ultralong waves can be stabilized at amplitude values differing up to one hundred meters of geopotential height while no correlated change in the patterns of zonal wind is observed. This property emerges from all the available statistics of low-frequency variability (see references above), and a further illustration is provided by the example presented in section 2.

The above property imposes severe constraints on possible dynamical interpretations. Linear theories based on the interference between traveling and stationary modes can, in line of principle, account for the observed amplitude excursion but imply the existence of a component of progressive phase, which is not observed. The extension of linear wave theories to include the nonlinearity arising from the interaction with zonal flow via momentum drag (Charney and Devore 1979;

Corresponding author address: Dr. Piero Malguzzi, Istituto FISBAT, Area di Ricerca CNR, via Gobetti 101, 40129 Bologna, Italy.

Legras and Ghil 1985) does not solve the problem since either of these theories predict major changes of the zonal wind, also not observed. In earlier papers on the subject we have shown that wave–wave interaction can, in line of principle, account for the above observational properties. In particular, with the help of extremely simplified models of atmospheric general circulation, we have shown that the meridional gradient of the "meridional contribution to vorticity," $\partial_y \partial_{yy} \Psi$, is capable of producing a wave self-non-linearity able to confine, through a mechanism of nonlinear resonance bending, stationary solutions in which the amplitude of the perturbation field ranges several tens of meters of geopotential height for fixed zonal wind. In order to keep the mathematical treatment of such physical process as simple as possible (minimal), it turns out convenient to "shape" the basic nonlinearity by means of an appropriate latitudinal function $g(y)$ and work in terms of a single longitudinal harmonic mode (in slight detuning from resonance). However, in the previous papers we did not provide an explicit physical justification for the use of such a projection, nor did we try to move toward more realistic representations of atmospheric planetary flows. In this work we address both questions: we will find numerically the stationary solutions of a quasigeostrophic barotropic model where the latitudinal structure is not preassigned and several modes in longitude are retained. We will show that the expected phenomenology of resonance bending is indeed found (section 3); we will then extend the BMSS analysis to models that are vertically continuous (sections 4–7), finding that it is possible to sustain topographically forced stationary waves of very different amplitudes with minor differences in form drag.

2. The phenomenology of a winter case

To illustrate the typical physical phenomenon that we want to model, let us consider National Meteorological Center Northern Hemisphere winter 500-mb geopotential height data for the winter 1962/63. These data have a 5° by 5° resolution covering the period starting 1 December–28 February. For this winter the time mean circulation is presented in Fig. 1. By visual inspection it can be seen that the large-scale circulation bears a strong signature of the zonal wavenumber 3 with relevant ridges upstream from the Rocky Mountains, the eastern Atlantic, and the Siberian region. To follow the time evolution of this pattern, we have considered first a latitude average of the geopotential height between 45° and 75°N. Then, we have computed the projection of the resulting one-dimensional field onto zonal wavenumber 3, obtaining the amplitude and phase of this Fourier component. In Figs. 2a and 2b we present the time behavior of these quantities while in Fig. 2c we show the behavior of the geostrophic wind in the same latitude belt. The figures show clearly that

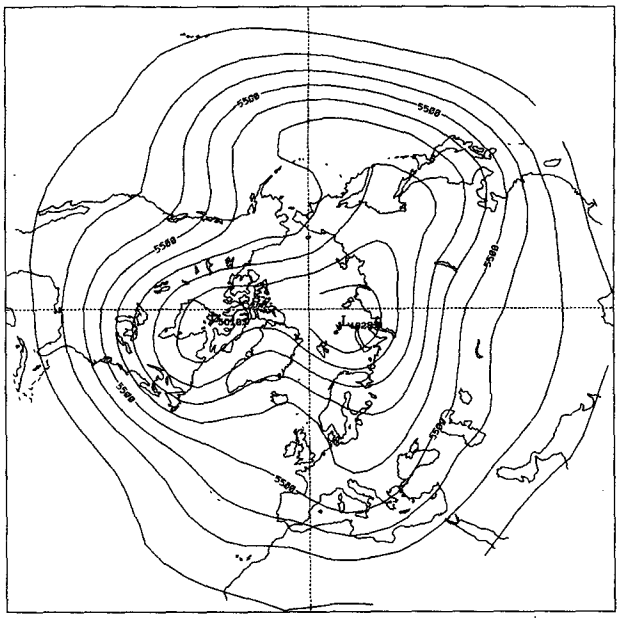

FIG. 1. Northern Hemisphere 500-mb geopotential height averaged in time from 1 Dec 1962–28 Feb 1963. Contour interval is 100 m.

the wave amplitude undergoes fluctuations of more than 100 m, while the zonal-mean zonal wind shows fluctuations of a few meters per second scarcely correlated with the wave behavior. As pointed out by Hansen and Sutera (1987), the lack of correlation extends to other zonally averaged parameters, such as the meridional and vertical shear of the zonal wind. Looking from day 35 onward, the growth of the wave occurs in a 10-day period, giving an e-folding time of approximately 4 days. Finally, we may recognize that after the growth stage there is a long period (about 25 days) where the amplitude of the wave remains larger than 100 m with a nearly fixed phase; this kind of behavior is not restricted to this particular winter but is rather typical of the Northern Hemisphere winter circulation, as documented by Hansen and Sutera (1986).

This phenomenology calls for an explanation that, in our opinion, cannot be obtained by a judicious application of linear wave–mean flow theories of the kind discussed in the previous section. In the next sections we will show evidence that theories can be accommodated when wave–wave interaction is accounted for.

3. The nonlinear resonance: A numerical example

In this section we consider the problem of estimating the stationary solution of a barotropic model written in spherical coordinates.

The main question that we address is the following. BMSS introduced the concept of resonance folding for a barotropic, topographically forced model by assum-

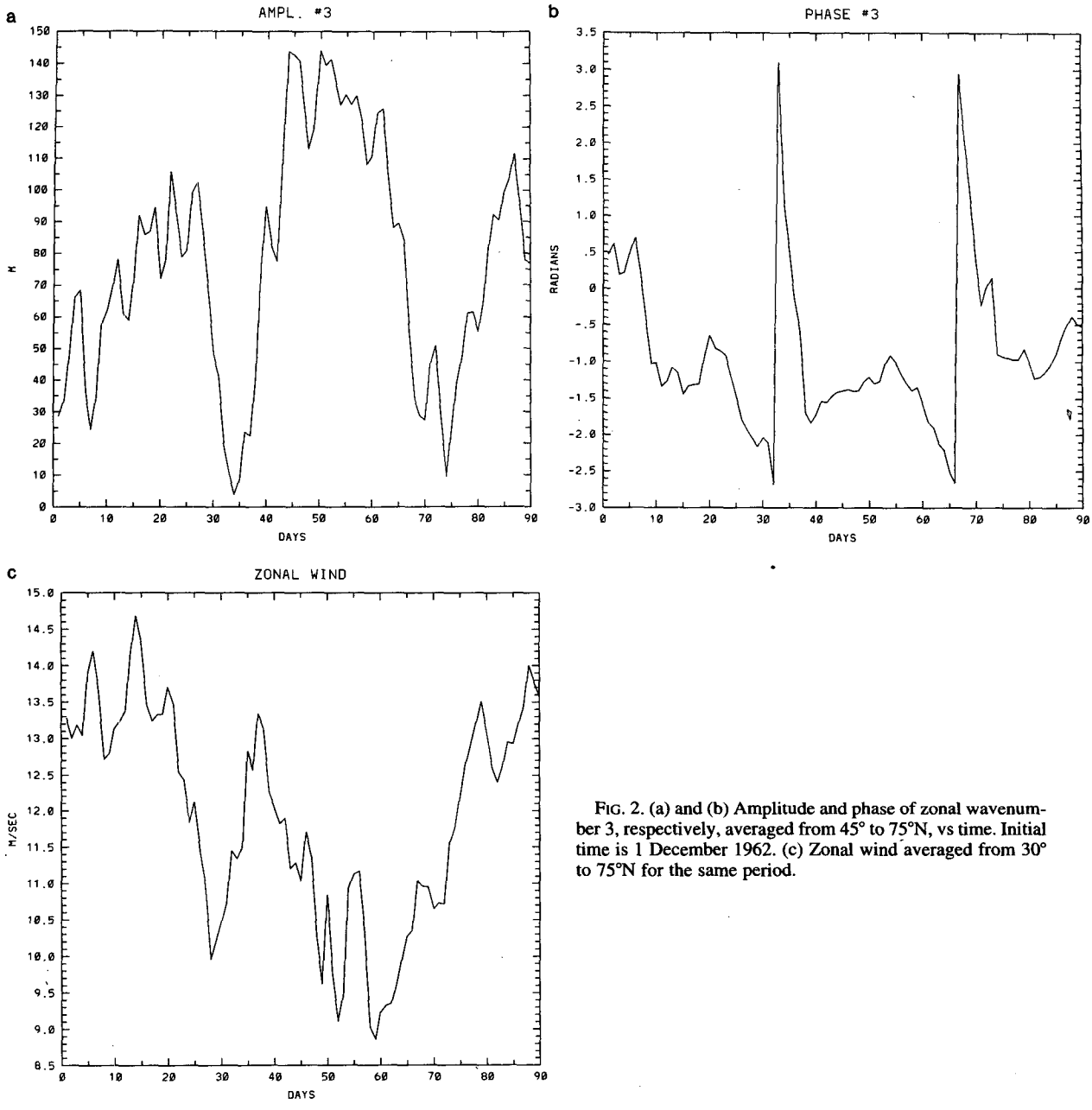

FIG. 2. (a) and (b) Amplitude and phase of zonal wavenumber 3, respectively, averaged from 45° to 75°N, vs time. Initial time is 1 December 1962. (c) Zonal wind averaged from 30° to 75°N for the same period.

ing that the streamfunction of the problem could be written as

$$\Psi \approx -Uy + g(y) \sum_{n=1}^{\infty} A_n e^{ik_n x}, \qquad (1)$$

where U is a constant and g such that

$$\delta = -\frac{3}{L_y} \int_0^{L_y} g g_y g_{yy} dy \neq 0. \qquad (2)$$

In that paper, g was left undetermined. Subsequently, in the reply to Källén and Reinhold (1988), it was suggested that g could be determined by solving the following Sturm–Liouville problem:

$$g_{yy} + [k^2 - V(y)]g = 0, \qquad (3)$$

with g zero at the latitudinal walls. The objection that was raised to this procedure is that, for U constant, the solution of the previous equation leads to trigonometric functions for which δ is zero, therefore, concluding that no resonance fold can occur. In a β channel, U constant

corresponds to a superrotation on a spherical earth, while U constant in spherical geometry allows meridional structures that are not trigometric functions. Thus, in spherical geometry we can presumably have δ different from zero even in the case of U uniform. To make explicit these ideas, we present in this section some numerical solutions of the barotropic equation for the perturbation field with no assumption concerning the latitudinal structure but retaining that the perturbation field be zero at the walls. The latter implies that, as mentioned in the introduction, some meridionally confining mechanism is operating.

We start from the barotropic, stationary, potential vorticity conservation equation written in spherical coordinates and in dimensionless form:

$$J(\Psi, \nabla^2\Psi + f + h) = -\nu_E\nabla^2\Psi + \nu_{sd}\nabla^4\Psi, \quad (4)$$

where the classic quasigeostrophic scaling is assumed. The length, velocity, and timescale are 1000 km, 10 m s^{-1}, and 10^5 s, respectively; the Rossby number Ro based on the Coriolis parameter computed at 45°N is 0.1. The height scale H is assumed to be 10 km. Accordingly, a dimensionless value of 1.0 for the orographic elevation corresponds to 1000 m of real height, since orography scales with the product $H\cdot$Ro. In (4) the following symbols and definitions have been introduced:

∇^2	$1/a^2\cos(\phi)\,\partial_\phi[\cos(\phi)\partial_\phi] + 1/a^2\cos^2(\phi)\,\partial^2/\partial\lambda^2$,
a	6.37 rescaled radius of the earth,
ϕ	latitude,
λ	longitude,
$J(\Phi, \tau)$	$1/a^2\cos(\phi)\,(\partial_\lambda\Phi\partial_\phi\tau - \partial_\phi\Phi\partial_\lambda\tau)$,
f	$2\Omega\sin(\phi)$, $\Omega = 2\pi/0.864$,
$h(\lambda, \phi)$	rescaled orography,
ν_E	rescaled Ekman dissipation coefficient,

where ν_{sd} is the coefficient of a superdissipative term, which has been included to prevent the occurrence of noisy numerical solutions.

Our goal is to find the numerical solutions for a fixed meridional profile of the zonal wind. Hence, we decompose the streamfunction into zonal and eddy part as follows,

$$\Psi = -\int_{\phi_0}^{\phi} Ua\,d\phi + \sum_{n=1}^{NT}\Psi_n(\phi)e^{in\lambda} + \text{c.c.}, \quad (6)$$

and solve the equation satisfied by the eddy part. Similarly, orography is decomposed in Fourier series along latitude circles:

$$h = \sum_{n=1}^{NT} h_n(\phi)e^{in\lambda} + \text{c.c.}$$

Since both amplitude and phase of wavenumber n are, in general, dependent on latitude, h_n will be a complex function. However, our interest is on the role of nonlinearity in near-resonant conditions and, therefore, we restrict this analysis to the idealized but simple case in which orography is formed by a single Fourier component, say, $n = n_R$, with a real meridional profile. Consistently, with the analysis of the previous section, the topographic wavenumber is then set to $n_R = 3$, and its meridional profile to a sine function vanishing at the lateral walls with amplitude h_0.

The Fourier coefficients of the eddy streamfunction field are discretized by defining a meridional grid of J points equally spaced. In order to better compare results with the minimal theory of BMSS, in the numerical solutions presented hereafter we spectrally truncate after zonal wavenumber $NT = 2n_R = 6$. Meridional resolution is set to $J = 20$. In Part II of the present work (in preparation) we will investigate the dependency of the numerical solution on parameters such as the meridional and zonal truncation, channel width, topographic height, and others. We anticipate here that by increasing the resolution up to $NT = 20$ and $J = 80$ no significant changes will be observed in the qualitative nature of the solutions.

Numerical solutions of the resulting set of nonlinear equations are found by following a solution curve with the pseudoarclength continuation method of Newton–Keller. This method has already been applied to a similar problem by, for instance, Legras and Ghil (1985), to which we address the reader for a description of the technique. Here, we briefly sketch the basic idea that consists of the iteration of the following two steps: (i) starting from a known solution for a certain value of an external parameter, say u, we obtain a guess for the solution at the new value $u + du$ by linear extrapolation along the tangent to the solution curve at u, and (ii) with several Newtonian steps we project the linear guess back to the solution curve. Convergence is checked by substituting the solution vector into the equations. The occurrence of singular points (points where derivatives with respect to u become infinite) is treated automatically by changing the sign of du. Both steps require the computation of the Jacobian matrix, which is performed numerically. The algorithm has proved effective in following solution curves with very complicated folding in high-dimensional phase space.

We now define a family of zonal wind profiles $U(\phi)$ in terms of the continuous parameter u. We assume the following definition:

$$U(\phi) = u\cdot P(\phi),$$

where $P(\phi)$ is a meridional profile with maximum amplitude one. For the purpose of the present paper we choose two particular forms of P in a 30° wide channel centered at 45°N, namely, a constant wind profile and a sine function with zeros at 25° and 75°N. A channel width of this size compares well with the

ones chosen by Charney and Eliassen (1949) and Charney and Devore (1979), with which BMSS wished to compare results. Moreover, the zonal flow is barotropically stable with no zero-wind lines (which could make stationary solutions singular) present in the domain.

The results are presented in Figs. 3a–c for the case of P constant and $h_0 = 0.04$, $\nu_E = 0.01$, $\nu_{sd} = 0.002$. Figure 3a shows the maximum amplitude of zonal wavenumber 3 (upper curve) and 6 (lower curve) as a function of the zonal wind speed u, Fig. 3b reports the phase of zonal wavenumber 3 computed in at the center of the channel, and Fig. 3c shows the eddy streamfunction field obtained when $u = 1.32$. The resonance curve bends to the right, and a region of multiple equilibria of mean zonal wind is found between 13.3 and 13.5 m s^{-1}. Zonal wavenumber 6 attains a much smaller amplitude than the orographic wavenumber, indicating that the convergence with increasing longitudinal resolution should be fast. The eddy streamfunction field presents a meridional structure particularly simple, with no appreciable

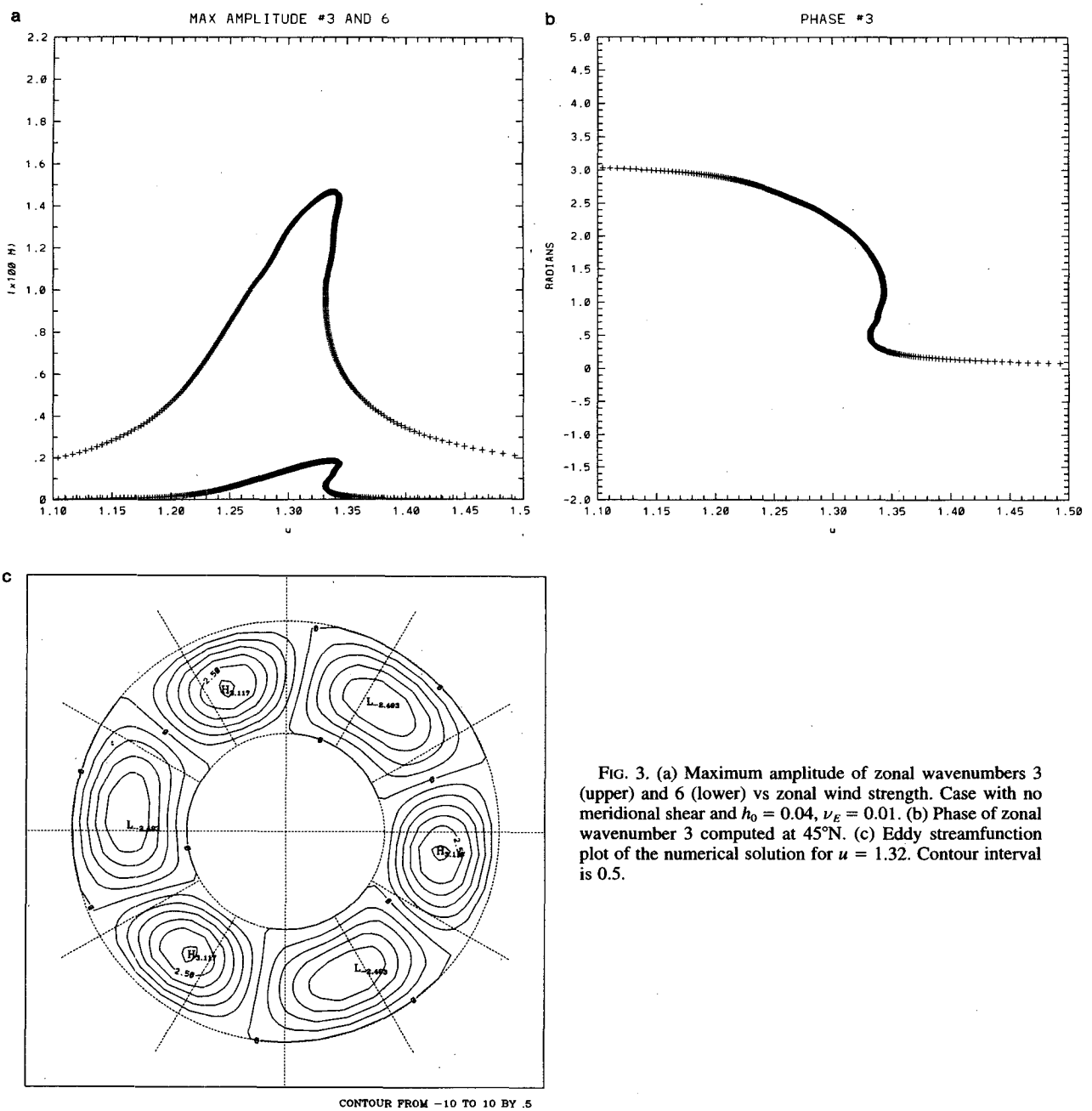

FIG. 3. (a) Maximum amplitude of zonal wavenumbers 3 (upper) and 6 (lower) vs zonal wind strength. Case with no meridional shear and $h_0 = 0.04$, $\nu_E = 0.01$. (b) Phase of zonal wavenumber 3 computed at 45°N. (c) Eddy streamfunction plot of the numerical solution for $u = 1.32$. Contour interval is 0.5.

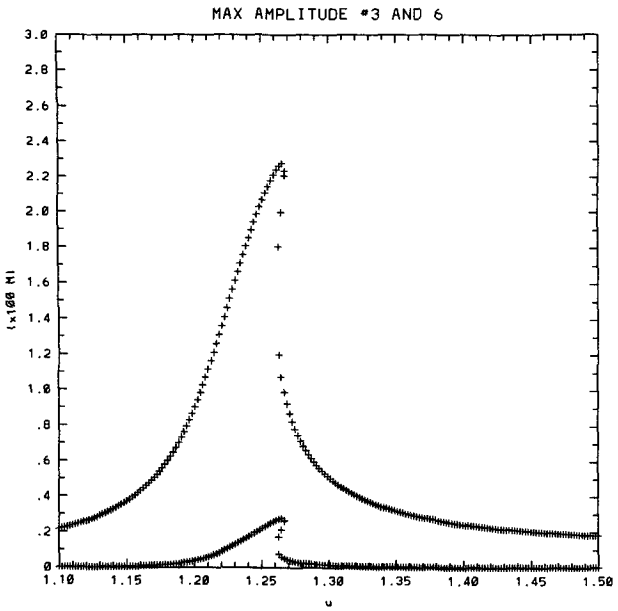

FIG. 4. Prediction of the weakly nonlinear theory of BMSS for the case in Fig. 3a.

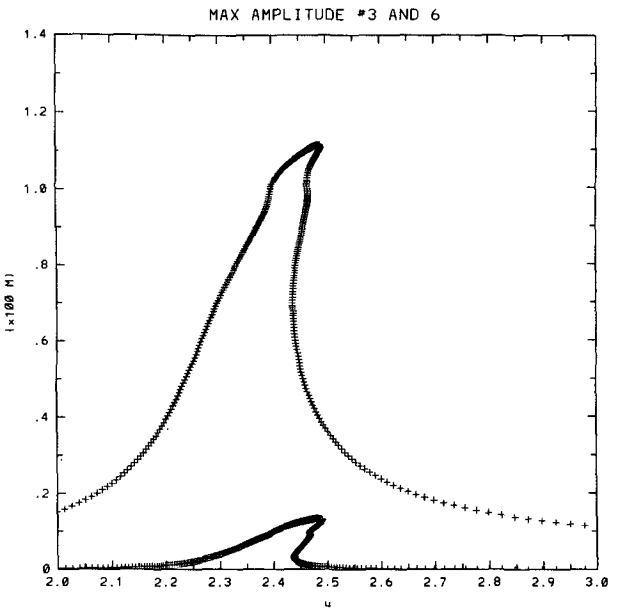

FIG. 5. As in Fig. 3a but for the case of jetlike zonal wind (see text) and $h_0 = 0.02$, $\nu_E = 0.01$.

momentum flux. The longitudinal structure is a succession of steep anticyclones, lying upstream of mountain ridges, and broader cyclones, which is an indication of the nonlinear nature of the solution. These qualitative features of the solution do not change along the resonance curve.

We now try to make a quantitative comparison with the predictions of BMSS theory. To this end, we must compute the parameters given by (12) of BMSS [see also our (13)], where we define the function $g(y)$ as the meridional structure of zonal wavenumber 3 obtained from the numerical solution previously discussed. The parameter δ turns out to be roughly -0.2, with a square of the same order of magnitude as the previously set h_0 and ν_E. We then solve (22) of BMSS, where the detuning from resonance is computed as difference from the orographic and stationary wavenumber, which is based on the Rossby wave dispersion, and where the orographic amplitude is obtained by projecting the meridional structure of the topography onto $g(y)$. The results are presented in Fig. 4. The comparison with the corresponding Fig. 3a can be considered very satisfactory, given the simplifications introduced in BMSS; in particular, the theoretical curve reaches higher amplitudes, and is less bended, than the numerical one.

We continue our presentation of numerical results in Figs. 5 and 6, where the profile P of the zonal wind has been fixed to a sine function, thus, taking into account strong potential vorticity gradients associated to the zonal wind. Figure 5 refers to a case with very small dissipation and orography ($h_0 = 0.02$, $\nu_E = 0.01$, $\nu_{sd} = 0.002$), while Fig. 6 shows a typical solution curve obtained for more realistic values of the parameters ($h_0 = 0.2$, $\nu_E = 0.08$, $\nu_{sd} = 0.01$). As was the case with P constant, the curve in Fig. 5 is obtained when the parameters scale according to BMSS theory, while the case in Fig. 6 is clearly out of the range of validity of

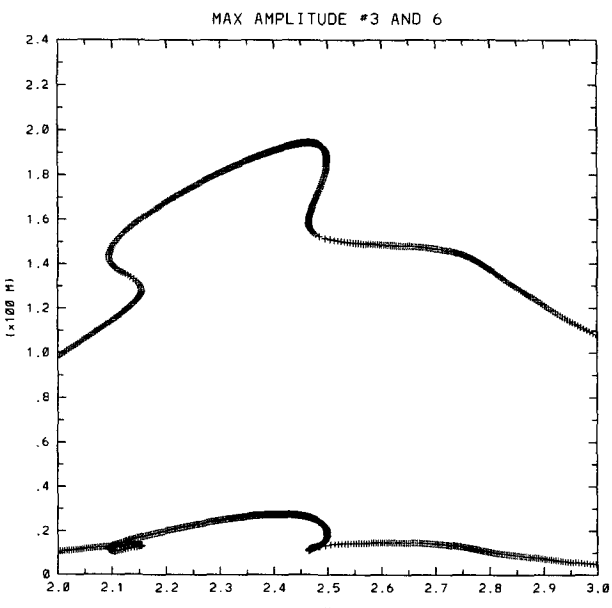

FIG. 6. As in Fig. 5 but for $h_0 = 0.2$, $\nu_E = 0.08$.

the theory. Multiple stationary solutions are, however, still observed.

We conclude this section with some observations.

(i) As for the case of the weakly nonlinear theory of BMSS, the Jacobian of the eddy streamfunction with orography does not play any relevant role in the numerical solutions. This has been checked by comparing numerical solutions with and without such a term. The occurrence of wavenumber $2n_R$ in the solution is then imputable to wave–wave interaction, which is the only nonlinearity present in our model.

(ii) The above dissipation coefficients correspond to very long timescales; even in the case of Fig. 6, an Ekman dissipation timescale shorter than 14 days would almost eliminate multiple solutions. However, the barotropic model grossly overestimates both Ekman and orographic forcings; in a baroclinic framework, both forcings are proportional to low-level zonal wind and streamfunction, which attain significantly smaller magnitudes than vertically averaged quantities. We will see in Part II that the numerical solutions of the two-layer model show bended resonances with more realistic values of topography and dissipation. Meanwhile, in the following sections we again apply BMSS theory and show that, in a vertically continuous baroclinic model, stationary waves of very different amplitude are associated with small changes in Ekman dissipation and form drag.

(iii) The starting point for the numerical procedure consists of zero amplitude for u far away from linear resonance. This algorithm cannot capture other eventual solution curves; unless, we define a first guess very close to the isolated branch. This may be a problem particularly in the case of Fig. 6, where BMSS theory does not apply.

4. The vertically continuous model

We consider the quasigeostrophic potential vorticity conservation:

$$(\partial_t + \Psi_x\partial_y - \Psi_y\partial_x) \times \left[\nabla^2\Psi + \beta y + \frac{1}{\rho_s}\partial_z\left(\frac{\rho_s}{S}\partial_z\Psi\right)\right] = 0, \quad (7)$$

where now ∇^2 denotes the Laplacian operator in the cartesian coordinates x and y, β the meridional gradient of the Coriolis parameter, Ψ the quasigeostrophic streamfunction, $\rho_s(z)$ the background density profile, and $S(z)$ the static stability profile. The boundary condition at $z = 0$ is given by the thermodynamic equation

$$(\partial_t + \Psi_x\partial_y - \Psi_y\partial_x)\Psi_z + Sw = 0, \quad (8)$$

where w denotes the vertical velocity, which is related to the orographic elevation $h(x, y)$ and to Ekman pumping by (see Pedlosky 1979)

$$w = \Psi_x h_y - \Psi_y h_x + \frac{E_v^{1/2}}{2\mathrm{Ro}}\nabla^2\Psi, \quad z = 0, \quad (9)$$

where Ro and E_v denote the Rossby and Ekman number, respectively. As an upper boundary condition we assume unbounded domain with finite energy density when $z \to \infty$; that is, $\rho_s\Psi^2 \to 0$.

All physical quantities appearing in (7)–(9) are dimensionless: we assume the same physical scales introduced in section 3. In the following we will write the background density as $\rho_s = \exp(-z/D)$, where the density height scale D is set to 0.9 (9 km).

Following BMSS, we expand the streamfunction onto a basis of orthonormal meridional structures and truncate to a single mode denoted by $g(y)$. Hence,

$$\Psi = -U(z)y + g(y)\psi(x, z, t) + \cdots, \quad (10)$$

where $g = 0$ at the boundaries and where the zonal and meridional mean wind profile, denoted by $U(z)$, has been separated off. By definition, the zonal average of ψ must be zero. By substituting (10) into (7)–(9), and by projecting the resulting equations on $g(y)$, we obtain

$$(\partial_t + U\partial_x)\left[\psi_{xx} - \alpha^2\psi + \frac{1}{\rho_s}\partial_z\left(\frac{\rho_s}{S}\psi_z\right)\right] + \beta\psi_x - \frac{1}{\rho_s}\psi_x\partial_z\left(\frac{\rho_s}{S}U_z\right) + \delta\psi\psi_x = 0 \quad (11)$$

$$\psi_{zt} + U\psi_{zx} - U_z\psi_x + SU\hat{h}(ik_0e^{ik_0x} + \text{c.c.}) + S\frac{E_v^{1/2}}{2\mathrm{Ro}}(\psi_{xx} - \alpha^2\psi) = 0, \quad z = 0, \quad (12)$$

where

$$\alpha^2 = \int g_y^2\,dy, \quad \delta = -3\int gg_yg_{yy}dy, \quad \int g^2dy = 1, \quad (13)$$

and where the projection over $g(y)$ of the orography has been assumed as sinusoidal with zonal wavenumber k_0 and amplitude $2\hat{h}$,; namely,

$$h(x, y) = g(y)\hat{h}(e^{ik_0x} + \text{c.c.}) + \cdots. \quad (14)$$

Since the atmospheric stationary wavenumber is around zonal wavenumber 3, we will limit the discussion in the rest of the work by considering only the orographic component with wavelength 10 000 km, which implies $k_0 = 0.628$.

In the following, we will assume that the parameter δ is a small number and that the solution of (11) and (12) can be expanded in a power series of δ as follows:

$$\psi = \psi^{(0)} + \delta\psi^{(1)} + \delta^2\psi^{(2)} + \cdots. \quad (15)$$

As shown by BMSS, resonance bending can be achieved by balancing, at the second order in δ, non-

linearity with orographic forcing and dissipation. Thus, the appropriate scaling of dissipation and orography is

$$\frac{E_v^{1/2}}{2\mathrm{Ro}} = \delta^2\nu, \quad \hat{h} = \delta^2 h_0, \tag{16}$$

where ν and h_0 are numbers of order one.

At the lowest order in δ, the stationary zero order solution $\psi^{(0)}$ of (11) and (12) can be written as

$$\psi^{(0)} = A(X)f_0(z)e^{ikx} + \text{c.c.}, \tag{17}$$

where $f_0(z)$ satisfies the following eigenvalue problem:

$$U\left[(-k^2-\alpha^2)f_0 + \frac{1}{\rho_s}\partial_z\left(\frac{\rho_s}{S}\partial_z f_0\right)\right] + \beta f_0 - \frac{f_0}{\rho_s}\partial_z\left(\frac{\rho_s}{S}\partial_z U\right) = 0$$

$$U\partial_z f_0 - f_0\partial_z U = 0, \quad z = 0, \tag{18}$$

and where $A(x)$ denotes an arbitrary amplitude that, in near-resonant conditions, will be the function of the slow scale $X = \delta^2 x$. The eigenvalue is given by the stationary wavenumber $k^2 + \alpha^2$. In the next section we shall discuss in detail the solution of (18) for realistic profiles of $U(z)$ and $S(z)$.

At the first order in δ, the stationary solution of (11) and (12) turns out to be

$$\psi^{(1)} = A^2 f_1(z)e^{2ikx} + \text{c.c.}, \tag{19}$$

where $f_1(z)$ satisfies the forced problem

$$U\left[(-4k^2-\alpha^2)f_1 + \frac{1}{\rho_s}\partial_z\left(\frac{\rho_s}{S}\partial_z f_1\right)\right] + \left[\beta - \frac{1}{\rho_s}\partial_z\left(\frac{\rho_s}{S}\partial_z U\right)\right]f_1 = -\frac{1}{2}f_0^2$$

$$U\partial_z f_1 - f_1\partial_z U = 0, \quad z = 0. \tag{20}$$

Finally, at the second order in δ, (11) and (12) become

$$U\partial_x\left[\psi_{xx}^{(2)} - \alpha^2\psi^{(2)} + \frac{1}{\rho_s}\partial_z\left(\frac{\rho_s}{S}\partial_z\psi^{(2)}\right)\right] + \left[\beta - \frac{1}{\rho_s}\partial_z\left(\frac{\rho_s}{S}\partial_z U\right)\right]\partial_x\psi^{(2)} + \psi^{(1)}\psi_x^{(0)} + \psi^{(0)}\psi_x^{(1)} + 2U\psi_{xXX}^{(0)} = 0 \tag{21}$$

$$U\psi_{xz}^{(2)} - U_z\psi_x^{(2)} + SUh_0(ik_0e^{ik_0x} + \text{c.c.}) + S\nu(\psi_{xx}^{(0)} - \alpha^2\psi^{(0)}) = 0, \quad z = 0, \tag{22}$$

where the x derivatives have been expanded as follows:

$$\partial_x \to \partial_x + \delta^2\partial_X, \quad \partial_{xx} \to \partial_{xx} + 2\delta^2\partial_{xX} + O(\delta^4), \tag{23}$$

and where x and X must be considered as independent variables. Equations (21) and (22) have a homogeneous part formally identical to the lowest-order problem (18); hence, as typical in perturbation problems, the necessary and sufficient condition for the solvability of (21) and (22) is that the projection of the forcing term on the solution of the lowest-order problem be zero. Thus,

$$\int_0^{L_x}\int_0^{\infty} f_0\frac{\rho_s}{U}[(21)\cdot e^{-ikx}]dxdz = 0. \tag{24}$$

By means of a double integration by parts, f_0 and $\psi^{(2)}$ can be exchanged in the double z-derivative term appearing in (24), at the price of considering two boundary terms that involve the quantity $\partial_x(U\partial_z\psi^{(2)} - U_z\psi^{(2)})$ computed at $z = 0$. This quantity can be written, after (22), in terms of $\psi^{(0)}$ and orographic elevation. Once the double integration by parts is performed, $\psi^{(2)}$ is eliminated from condition (24), leaving the following relationship to be satisfied:

$$ikA^2A^*\int_0^{\infty} f_1 f_0^2\frac{\rho_s}{U}dz - 2k^2A_X\int_0^{\infty} f_0^2\rho_s dz + f_0(0)h_0ik_0e^{i(k_0-k)x} - \nu(k^2+\alpha^2)\times\frac{f_0(0)^2}{U(0)}A = 0. \tag{25}$$

The condition of "near resonance" can thus be expressed as

$$(k_0 - k)x = \Delta k\delta^2 x = \Delta kX, \tag{26}$$

where Δk, the detuning parameter, is an order-one quantity. The solution of (25) is then written in the form

$$A(X) = A_0e^{i\Delta kX}, \tag{27}$$

where the complex constant A_0 satisfies the following algebraic equation:

$$I|A_0|^2A_0 - 2k\Delta kA_0 + f_0(0)h_0 + i\frac{\nu}{k}\frac{f_0(0)^2}{U(0)}(k^2+\alpha^2)A_0 = 0$$

$$I = \int_0^{\infty} f_1 f_0^2\frac{\rho_s}{U}dz, \quad \int_0^{\infty} f_0^2\rho_s dz = 1, \tag{28}$$

and where we have exploited the freedom to choose a normalization for f_0. By solving (28), the computation of the zero- and first-order solutions is then completed. As we will see in the next sections, (28) will in general admit multiple solutions. We notice that in the limit $\nu \to 0$ and $h_0 \to 0$ (28) still admits multiple steady states; namely, $A_0 = 0$ and $A_0^2 = 2k\Delta k/I$. Hence, the nonlinear nature of our problem implies multiple free solutions. The first one is a pure axisymmetric flow, while the

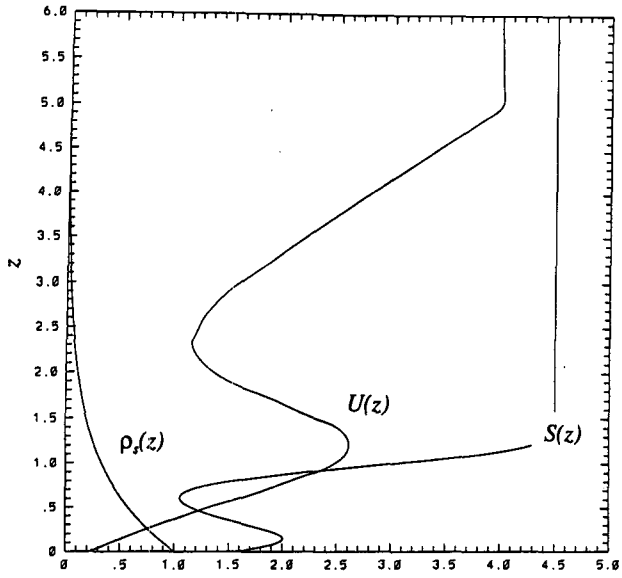

FIG. 7. Vertical profiles of density (ρ_s), static stability (S), and zonal wind (U) in dimensionless units.

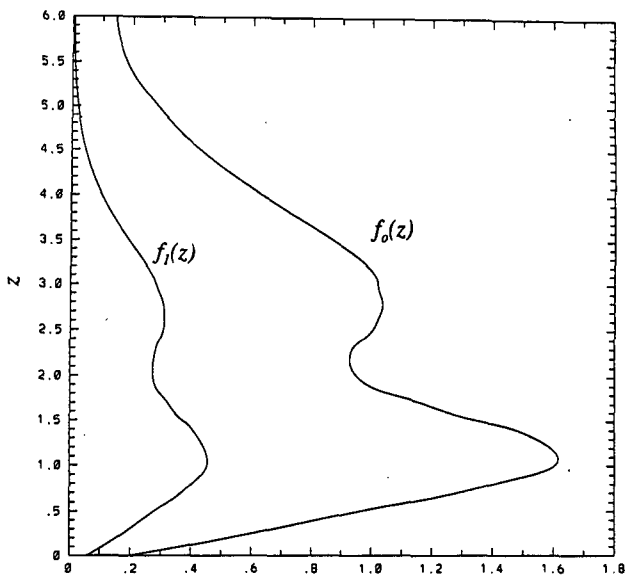

FIG. 8. Vertical profiles of zero-order (f_0) and first-order (f_1) solution corresponding to the first trapped eigenmode.

other two are finite amplitudes waves with phase opposition. The inclusion of topography and dissipation slightly modifies the zonally symmetric solution with a small amplitude wave, while the large amplitude solutions assume a definite phase relative to orography (see section 6).

5. Vertical structure problem

The solution of the lowest-order problem (18) gives the vertical structure of stationary and linear Rossby waves superimposed on the zonal wind $U(z)$, and for a frictionless atmosphere characterized by background density and static stability function of the vertical coordinate. It is well known that this problem admits vertically trapped or propagating solutions, essentially depending on the strength of the mean zonal wind. Since we are interested, in the present work, in modeling the amplification of tropospheric waves in winter conditions, we will limit ourselves to trapped solutions for which $\rho_s f_0^2$ goes to zero as $z \to \infty$.

In Fig. 7 we report the (dimensionless) vertical profiles chosen for density, zonal wind, and static stability. The wind profile has been obtained by averaging in latitude the observed structure of the midlatitude jet stream typical of winter conditions, as shown, for instance, by Lindzen (1990). Polynomial fits are used to interpolate the data so that vertical profiles and their derivatives are known at any vertical point. Above the height of 50 km and up to infinity, the zonal wind has been kept constant, with a smooth match with the wind below 50 km. The averaged zonal wind at $z = 0$ turns out to be roughly 2 m s^{-1}. The static stability parameter for winter conditions has been adapted from Gutowski (1985), which reports the Brunt–Väisälä frequency up to the height of 15 km. Above this height the static stability is kept as constant and equal to 4.5 dimensionless units, roughly three times the tropospheric value. Finally, the dimensionless value of β is set to

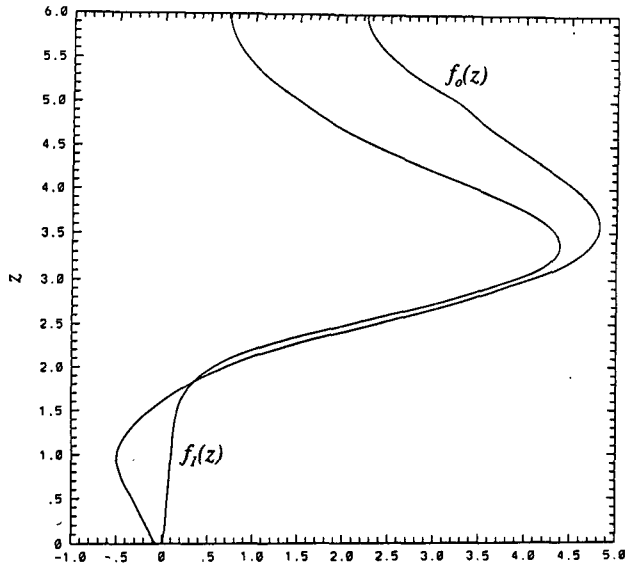

FIG. 9. As in Fig. 8 but for the second trapped eigenmode.

1.6, which corresponds to the physical value computed at 45°N.

Due to the complexity of the vertical profiles, (18) has to be solved numerically. This is done by defining a vertical grid of equally spaced points and by discretizing the vertical derivatives with a second-order centered scheme. This reduces (12) to a generalized eigenvalue problem, which can be solved for the eigenvalue $K^2 = k^2 + \alpha^2$. As an upper boundary condition, in the numerical code we impose $\partial_z f_0 = 0$ at $z = z_{max}$, implying the presence of a rigid lid. This artificial condition may somewhat influence structure and eigenvalue of trapped modes; however, the "robustness" of the numerical solution can be checked by increasing the value of z_{max}. Moreover, with U and S being constant above a certain height, the numerical solution can be compared to the exact solution that is known analytically as $z \to \infty$ (see Pedlosky 1979). It turns out that for $z_{max} = 8$ the fit between analytical and numerical solution is excellent in the range of values of z somewhat above 5 and somewhat below 8. We conclude that the artificial upper boundary condition does not affect trapped modes. With the above choice of vertical profiles, two trapped solutions are found that are characterized by eigenvalues $K_1^2 = 0.91$ and $K_2^2 = 0.66$.

Next, we solve the first-order problem (20) by using the two profiles of f_0 just found. The solution of (20) is also computed numerically by means of a scheme consistent with the one previously described. Before solving (20), the parameter k^2 (or α^2) must be specified. Since we want to be close to resonance, k must be close to k_0, the mountain wavenumber. Hence, the factor $4k^2 + \alpha^2$ in (20) can be replaced by $3k_0^2 + K_{1,2}^2$. The vertical structure of the zero- and first-order solutions and for the two trapped modes is shown in Figs. 8 and 9, respectively, where the zero-order solution has been normalized according to the last of (28). Clearly, the eigenmode in Fig. 9 propagates in the vertical through the jet stream and is trapped by the strong stratospheric westerlies; therefore, we shall restrict our study to the eigenmode in Fig. 8.

6. Amplitude equilibration

The amplitude of the stationary Rossby wave is determined by condition (28). In (28) we can consistently replace $k^2 + \alpha^2$ and k with K_1^2 and k_0, respectively; this leaves us with three unknown parameters: h_0, Δk, and ν. It turns out convenient to estimate the ratio $R = \nu/h_0$, which is a quantity independent of δ. In fact, after (16), we obtain

$$R = \frac{E_v^{1/2}}{2\mathrm{Ro}\hat{h}} = \frac{\left(\frac{2A_v}{f_C}\right)^{1/2}}{h_{max}}, \qquad (29)$$

where A_v denotes the vertical turbulent viscosity coefficient, f_C the Coriolis parameter computed at a central latitude, and h_{max} the amplitude of the zonal wavenumber three Fourier component of the earth orography in physical units. By assuming $A_v = 5$ $m^2 s^{-1}$ (Holton 1979) and $h_{max} = 300$ m, we get $R \approx 1$. However, in this way we are likely to overestimate real dissipative effects; in fact, in a baroclinic atmosphere, the insurgence of a secondary flow inside the planetary boundary layer will quickly spin down the vorticity at the top of the layer, thus reducing the efficiency of Ekman dissipation. In other words, it is not realistic to consider the effect of Ekman dissipation as "perturbative" over the amplitude of the streamfunction at $z = 0$. Hence, we will also investigate values of R smaller than one. Finally, the detuning of Δk can be easily expressed as a function of α^2 by the definition of the eigenvalue K_1^2:

$$\Delta k = \frac{k_0^2 + \alpha^2 - K_1^2}{2k_0\delta^2}. \qquad (30)$$

Thus, the uncertainty in the numerical value of α^2 is obviously reflected in the uncertainty in the knowledge of the detuning from resonance.

Figure 10a shows examples of solutions of (28) (modulus of A_0) as functions of Δk for some values of h_0 and $R = 0.5$, while Fig. 10b reports similar curves but for two different values of R and fixed h_0. For a fixed ratio between dissipation and orography, the resonance curves attain the same value of maximum amplitude at the same value of Δk; moreover, by decreasing h_0 (increasing δ) the resonance bends, increasing the region in the Δk space where multiple equilibration is found. Resonance bending is even more spectacular when R is decreased by only a small amount, as shown in Fig. 10b. Note also that resonance bent does not depend upon the sign of δ. Phase change through resonance, shown in Fig. 10c, indicates that, in the subresonant (superresonant) case, the wave tends to be in opposition (coincidence) of phase with orography. This phase behavior is very similar to what is shown by the numerical solutions of the previous section (see Fig. 3b). In Fig. 10 the dotted curve represents the amplitudes of two of the solutions of (28) obtained in the limit of $\nu \to 0$ and $h_0 \to 0$ (which have opposite phase), while the horizontal axes represent the axisymmetric solution. Thus, the inclusion of small topography and dissipation fixes the phases of all solutions and perturbs the zonally symmetric equilibrium. Moreover, it is easy to show that (e.g., Landau and Lifchitz 1969) the smaller and larger amplitude solutions are stable (at least for perturbations whose dynamics is approximated by the asymptotic theory) while the intermediate one is unstable. This instability is easily identified with a wave–wave interaction

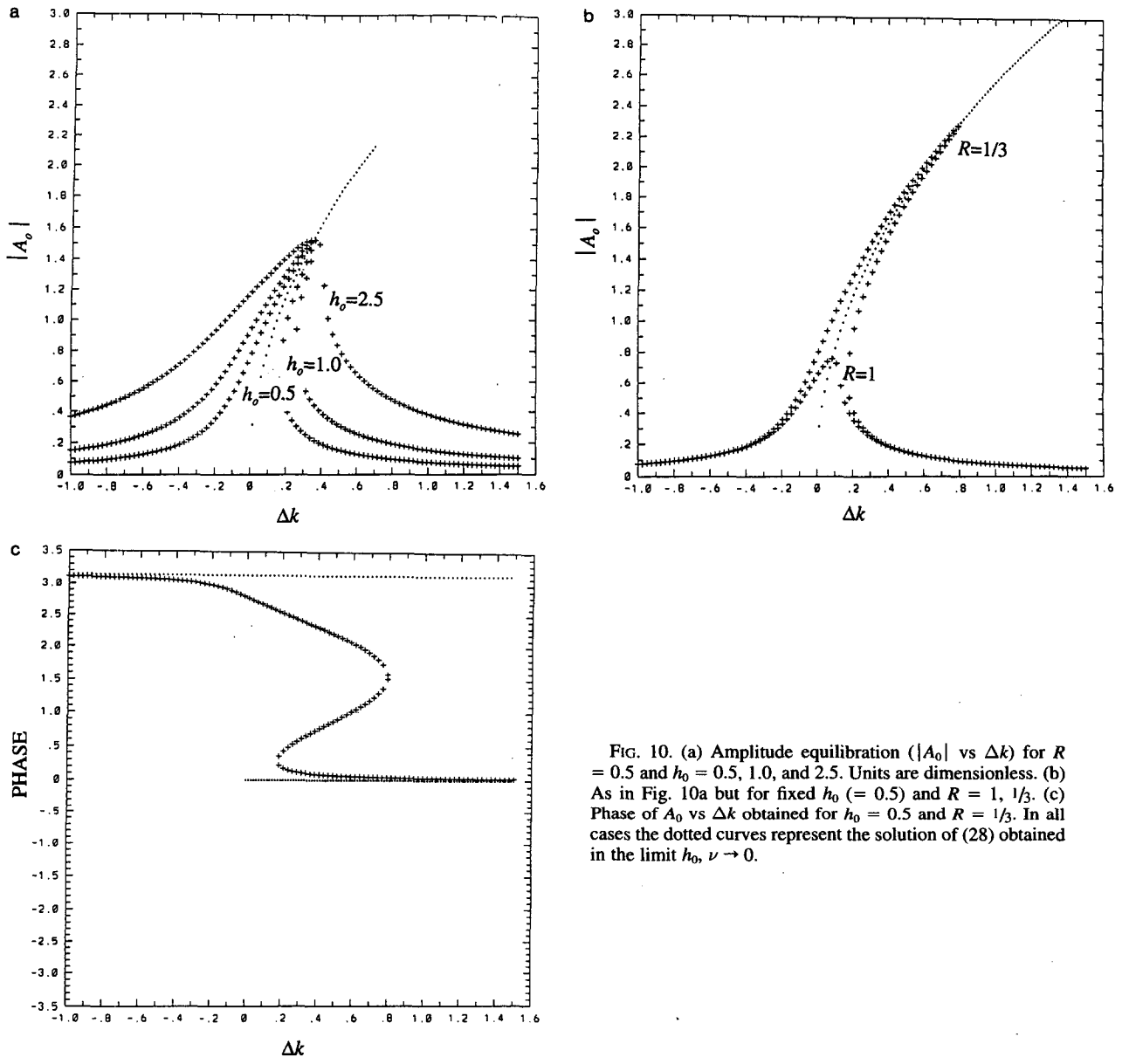

FIG. 10. (a) Amplitude equilibration ($|A_0|$ vs Δk) for $R = 0.5$ and $h_0 = 0.5$, 1.0, and 2.5. Units are dimensionless. (b) As in Fig. 10a but for fixed h_0 (= 0.5) and $R = 1, 1/3$. (c) Phase of A_0 vs Δk obtained for $h_0 = 0.5$ and $R = 1/3$. In all cases the dotted curves represent the solution of (28) obtained in the limit $h_0, \nu \to 0$.

instability with zero phase speed because of the presence of topography.

In Fig. 11 we report a plot of the zero- plus first-order streamfunction in the x–z plane, where parameters have been fixed at $h_0 = 0.5$, $R = 0.5$, and $\Delta k = 0.25$, for which three solutions exist. Mountain ridges are centered at the left and right bottom corners of the figure, while orographic depression is located at the center of the x-domain. The plot in Fig. 5 is relative to the high-amplitude solution, whose anticyclone lies just upstream of the mountain ridge, in agreement with observations. Note also that the effect of nonlinearity is to steepen the anticyclonic part of the solution, localizing the "blocking" pattern in a more realistic fashion. This particular aspect is the direct consequence of quadratic nonlinearity and has already been encountered in other studies (e.g., Malguzzi 1993). Again, the analogy with the numerical solutions presented in section 3 is clear.

7. Second-order correction and energetic

The second-order solution is governed by (21) and (22), with A given by (27) and (28). By substituting the following tentative expression

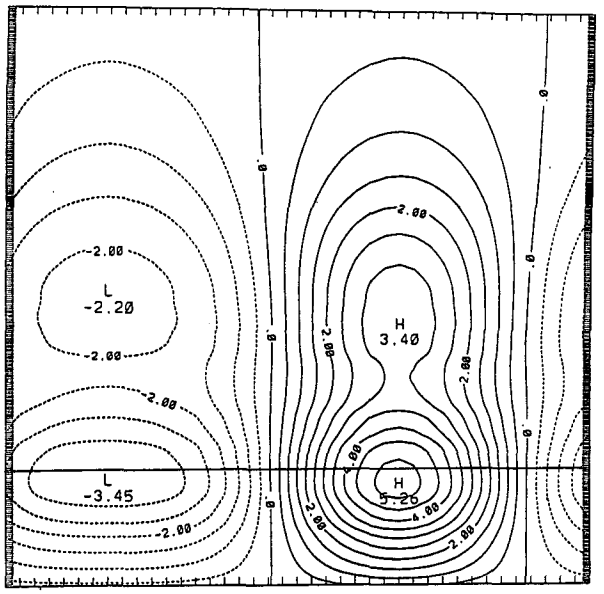

FIG. 11. Cross section in the $x-z$ plane of the (high amplitude) zero- plus first-order solution, obtained for $h_0 = 0.5$, $R = 0.5$, $\delta^2 = 0.3$, and $\Delta k = 0.25$. Units are dimensionless. The topographic ridge is centered at $x = 0$. The "tropopause" ($z = 1.2$) is marked by a horizontal solid line.

$$\psi^{(2)} = Af_2(z)e^{ikx} + \text{c.c.}, \quad f_2 \in \mathbb{C} \tag{31}$$

into (21) and (22) we get

$$U\left[(-k^2 - \alpha^2)f_2 + \frac{1}{\rho_s}\partial_z\left(\frac{\rho_s}{S}\partial_z f_2\right)\right] + \beta f_2 - \frac{f_2}{\rho_s}\partial_z\left(\frac{\rho_s}{S}\partial_z U\right) = -|A_0|^2 f_0 f_1 + 2Uk\Delta k f_0 \tag{32}$$

$$U\partial_z f_2 - f_2\partial_z U = -SUh_0\frac{A_0^*}{|A_0|^2} - iS\nu\frac{(k^2+\alpha^2)}{k}f_0, \quad z = 0. \tag{33}$$

The right-hand side of (33) can be rearranged, after (28), as

$$\frac{SU(0)}{f_0(0)}(I|A_0|^2 - 2k\Delta k), \tag{34}$$

which is a real expression. Hence, the right-hand side of (32) and (33) are both real, implying a real solution for $f_2(z)$. It is now clear that the solution up to the second order in δ is equivalently barotropic. This fact has important implications as far as the energetics of the solution is concerned: there is no available potential energy conversion in the interior of the domain to compensate for energy losses due to Ekman friction. In this respect, the present solution differs from the one of Benzi et al. (1986b), in which an order-two heat flux was present due to phase difference between zero- and second-order solutions. The physical difference is the presence, in Benzi et al. (1986b), of a form of internal dissipation which demanded for energy conversion also in the interior of the domain. We suggest that the westward tilt with height of stationary planetary waves, pointed out by some observational study (e.g., Dole 1982), may be imputable to some kind of internal dissipation; in the presence of Ekman pumping only, all energetic conversions take place inside the boundary layer, which is placed at $z = 0$ in the present study. We will return to this important point in Part II of the present work; we anticipate here that stationary solutions of the two-layer model indeed share this property.

A quick glance at the energetics of the streamfunction defined by (11) and (12) shows that our orographic waves are maintained against dissipation by form drag conversion, at least when the stationary state is reached. In fact, by averaging in x equation (11) multiplied by $\rho_s\phi$ we get

$$\partial_t\left[\rho_s\left(\frac{\overline{\psi_x^2}}{2} + \alpha^2\frac{\overline{\psi^2}}{2}\right) + \frac{\rho_s}{S}\frac{\overline{\psi_z^2}}{2}\right] = \partial_z\left[\frac{\rho_s}{S}\overline{\psi\psi_{zt}} - U\frac{\rho_s}{S}\overline{\psi_x\psi_z}\right] + \frac{\rho_s}{S}U_z\overline{\psi_x\psi_z}, \tag{35}$$

where the overbar denotes x average. Equation (35) states that the time derivative of kinetic plus potential energy of the eddy field, at a particular height inside the vertical domain, is the sum of a heat flux term plus the divergence of the vertical flux of total energy. The energy flux is the sum of two contributions, one of which is zero for stationary solutions. Hence, being the correlation between meridional wind and temperature zero in our case up to the second order, the pointwise energy balance is trivial. By further integrating (35) with respect to z, and by using the boundary condition (12), we finally obtain

$$\frac{d}{dt}(K_e + P_e) = \int_0^\infty \frac{\rho_s}{S}U_z\overline{\psi_x\psi_z}dz - \frac{E_v^{1/2}}{2\text{Ro}}(\overline{\psi_x^2 + \alpha^2\psi^2})|_{z=0} + U(0)\overline{\hat{h}\psi}|_{z=0}(ik_0e^{ik_0x} + \text{c.c.}). \tag{36}$$

Up to the second order in δ and for stationary solutions, (36) reduces to

$$2\nu f_0(0)^2|A_0|^2(k_0^2 + \alpha^2) = 2\text{Im}(A_0)k_0f_0(0)U(0)h_0, \tag{37}$$

which expresses the balance between energy dissipated in the Ekman layer and kinetic energy conversion from

zonal to eddy motion due to form drag, associated with phase shift between the low-level streamfunction and orography. Notice that the energy balance (37) is implied by the secular condition (28), as can be readily demonstrated by taking the imaginary part of (28) multiplied by A_0^*.

Hansen and Sutera (1987) have shown that the fluctuations of midlatitude planetary-scale wave amplitudes cannot be explained in terms of fluctuations of the vertically averaged zonal mean wind. This piece of evidence has always constituted a problem for barotropic theories of multiple equilibria, like those of Charney and Devore (1979) and BMSS, because relation (37) strongly correlates wave amplitude with form drag. However, in the vertically continuous model, the wave amplitude at the ground strongly depends on the wind speed there [the lower boundary condition (18) implies $f_0(0) \to 0$ when $U(0) \to 0$], making the vertically averaged zonal wind virtually independent on the eddy amplitude aloft. In fact, the barotropic theory of BMSS give values for both sides of (37) that are at least one order of magnitude larger than those obtained, with the same vertically averaged wave amplitude, in the baroclinic case. Thus, while the barotropic model is inconsistent with the above set of observations, the vertically continuous model does not suffer from the same hindrance.

The actual determination of the second-order correction is superfluous for our purposes and will not be performed. We point out only that (32) and (33) define a singular problem, being left-hand side identical to the zero-order problem (20). Nevertheless, the second-order problem admits infinite solutions, which can be obtained by neglecting one equation and by fixing arbitrarily one variable among the N ones forming the numerical scheme of (32) and (33).

8. Conclusions

In this paper we have discussed a possible mechanism that could generate part of the observed planetary-scale low-frequency variability. The mechanism rests on the assumption that low-frequency variability can be, along with other processes, a manifestation of the transition among planetary-scale weather regimes. We have shown that, by fixing the zonal wind profile, it is possible to find multiple stationary solutions of the perturbation field both in a numerically solved barotropic model and in a simple theory for a vertically continuous quasigeostrophic equation, in accordance with an earlier theory that we presented several years ago. The theory relies on the hypothesis that wave–wave nonlinearity is perturbative and that topographic and dissipative forcings are even smaller quantities. We do not have direct measures of such quantities for the atmospheric general circulation; however, as will be clear in Part II, even when generally accepted values of topographic elevation and Ekman timescale are chosen, the numerical solutions of our model show the classic bended resonance, which suggests that the ordering could be the one proposed here.

By applying the same theory to a vertically continuous atmosphere, we have shown that external Rossby waves can be maintained to finite (large) amplitude even in the absence of substantial heat fluxes, by balancing Ekman dissipation with a small mountain drag. Of course, the latter result should be substantiated by appropriate observational analysis, though some hints are already suggested by the work of Hansen (1988). We intend to pursue further these findings by judicious use of the observations along the above-discussed line.

Our multiple solutions have been obtained by solving only the eddy vorticity equation; no mention has been given to the equation of the zonal part. The equation for the zonal wind balances form drag, eddy stress terms, and an external forcing that usually assumes the form of $-\nu[U - U^*(y, z)]$, where U^* is a specified wind profile. From the mathematical point of view, our solutions are obtained in the limit in which the external forcing can be much larger than the other forcing terms. This is *precisely* the case of the weakly asymptotic theory of BMSS, where form drag and eddy momentum and heat fluxes are of second order. Thus, our multiple solutions correspond to the same zonal wind profile, unless there are reasons to believe that ν is second order as well. The above form of the external forcing has no sound physical justification; it simply represents a Newtonian relaxation toward an arbitrary profile that mimics many physical processes that may or may not be described by the quasigeostrophic vorticity equation (like eddy momentum flux by baroclinic eddies, ageostrophic effects on the mean meridional circulation, and so on) and that may be characterized by short timescales.

For the sake of clarity we have not fully discussed many related issues that we hinted at in the body of the paper and that we will address in a forthcoming one. In Part II of this work we will present an improved theoretical analysis, not based on meridional truncation, in which nonlinearity is explicitly evaluated and not parameterized by a δ term. We will also assess the limit of validity of the weakly nonlinear theory, through scaling arguments and comparisons with numerical solutions, and account for the robustness of the numerical results by considering different physical parameters—like channel width, zonal wind latitudinal profile, topography, and Ekman dissipation—both for the barotropic and a simple two-level baroclinic model.

Acknowledgments. Support for this work was provided by CEE Contracts EPOC-CT90-0012 and

EV5V-CT93-0259. The authors acknowledge partial support from GNFAO-CNR.

REFERENCES

Benzi, R., and A. Speranza, 1989: Statistical properties of low frequency variability in the Northern Hemisphere. *J. Climate,* **2,** 367–379.

——, and P. Malguzzi, 1992: Amplification and meridional confinement of stationary and quasi-stationary eddies in a two-layer model. *J. Atmos. Sci.,* **49,** 1585–1593.

——, P. Malguzzi, A. Speranza, and A. Sutera, 1986a: The statistical properties of general atmospheric circulation: Observational evidence and a minimal theory of bimodality. *Quart. J. Roy. Meteor. Soc.,* **112,** 661–674.

——, A. Speranza, and A. Sutera, 1986b: A minimal baroclinic model for the statistical properties of low-frequency variability. *J. Atmos. Sci.,* **43,** 2962–2967.

——, S. Iarlori, G. Lippolis, and A. Sutera, 1988: Steady nonlinear response of a barotropic quasi-unidimensional model to complex topography. *J. Atmos. Sci.,* **45,** 3313–3319.

Charney, J. G., and A. Eliassen, 1949: A numerical method for predicting the perturbations of the middle latitude westerlies. *Tellus,* **1,** 38–54.

——, and J. G. Devore, 1979: Multiple flow equilibria in the atmosphere and blocking. *J. Atmos. Sci.,* **36,** 1205–1216.

Dole, R. M., 1982: Persistent anomalies of the extratropical Northern Hemisphere wintertime circulation. Ph.D. thesis, Massachusetts Institute of Technology, 226 pp.

Gutowski, W. J., 1985: Baroclinic adjustment and midlatitude temperature profiles. *J. Atmos. Sci.,* **42,** 1733–1745.

Hansen, A. R., 1988: Further observational characteristics of bimodal planetary waves: Mean structure and transitions. *Mon. Wea. Rev.,* **116,** 386–400.

——, and A. Sutera, 1986: On the probability density distribution of planetary-scale atmospheric wave amplitude. *J. Atmos. Sci.,* **43,** 3250–3265.

——, and ——, 1987: The probability density distribution of the speed and horizontal and vertical shear of the zonal-mean flow. *J. Atmos. Sci.,* **44,** 1525–1533.

——, and ——, 1990: Weather regimes in a general circulation model. *J. Atmos. Sci.,* **47,** 380–391.

——, ——, and J. J. Tribbia, 1991: The relation of multiple flow regimes to the climatic error in general circulation models: Southern Hemisphere winter. *J. Atmos. Sci.,* **48,** 1329–1335.

Holton, J. R., 1979: *An Introduction to Dynamic Meteorology.* 2d ed. Academic Press, 391 pp.

Källén, E., and B. Reinhold, 1988: Comments on "The statistical properties of the general atmospheric circulation: Observational evidence and a minimal theory of bimodality." *Quart. J. Roy. Meteor. Soc.,* **114,** 269–272.

Landau, L., and E. Lifchitz, 1969: *Mécanique.* Editions MIR, 120 pp.

Legras, B., and M. Ghil, 1985: Persistent anomalies, blocking and variation in atmospheric predictability. *J. Atmos. Sci.,* **42,** 433–471.

Lindzen, R. S., 1990: *Dynamics in Atmospheric Physics,* Cambridge University Press, 310 pp.

Malguzzi, P., 1993: An analytic study on the feedback between large- and small-scale eddies. *J. Atmos. Sci.,* **50,** 1429–1436.

Pandolfo, L., and A. Sutera, 1991: Rossby waves in a fluctuating zonal mean flow. *Tellus,* **43A,** 257–265.

Pedlosky, J., 1979: *Geophysical Fluid Dynamic.* Springer-Verlag, 624 pp.